

PAPER • OPEN ACCESS

Characterization of the thorium-229 defect structure in CaF_2 crystals

To cite this article: S Takatori *et al* 2025 *New J. Phys.* **27** 043024

View the [article online](#) for updates and enhancements.

You may also like

- [Experimental search for the low-energy nuclear transition in \$^{229}\text{Th}\$ with undulator radiation](#)
A Yamaguchi, M Kolbe, H Kaser et al.
- [Proposal for precision determination of 7.8 eV isomeric state in \$^{229}\text{Th}\$ at heavy ion storage ring](#)
X Ma, W Q Wen, Z K Huang et al.
- [Surface physicochemical properties and decay of the low-lying isomer in the \$^{229}\text{Th}\$ nucleus](#)
P.V. Borisyuk, U.N. Kurel'chuk, O.S. Vasil'ev et al.



OPEN ACCESS

RECEIVED

7 November 2024

REVISED

9 March 2025

ACCEPTED FOR PUBLICATION

17 April 2025

PUBLISHED

28 April 2025






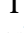




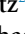
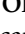
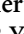
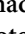


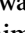
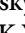

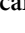
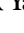




Original Content from
this work may be used
under the terms of the
[Creative Commons
Attribution 4.0 licence](#).

Any further distribution
of this work must
maintain attribution to
the author(s) and the title
of the work, journal
citation and DOI.



PAPER

Characterization of the thorium-229 defect structure in CaF₂ crystals

S Takatori^{1,*} , M Pimon² , S Pollitt² , M Bartokos² , K Beeks^{2,3} , A Grüneis² , T Hiraki¹ , T Honma⁴ , N Hosseini² , A Leitner² , T Masuda¹ , I Morawetz² , K Nitta⁴ , K Okai¹ , T Riebner² , F Schaden² , T Schumm² , O Sekizawa⁴ , T Sikorsky² , Y Takahashi⁵ , L Toscani De Col² , R Yamamoto¹ , T Yomogida^{5,6} , A Yoshimi¹  and K Yoshimura¹ 

¹ Research Institute for Interdisciplinary Science (RIIS), Okayama University, Tsushima-naka 3-1-1 Kita-ku, Okayama 700-8530, Japan

² Faculty of Physics, TU Wien, Vienna, Austria

³ Laboratory for Ultrafast Microscopy and Electron Scattering (LUMES), Institute of Physics, Ecole Polytechnique Fédérale de Lausanne (EPFL), Lausanne CH-1015, Switzerland

⁴ Japan Synchrotron Radiation Research Institute, 1-1-1 Kouto, Sayo-cho, Sayo-gun, Hyogo 679-5198, Japan

⁵ Department of Earth and Planetary Science, The University of Tokyo, Bunkyo-ku, Tokyo 113-0033, Japan

⁶ Nuclear Safety Research Center, Japan Atomic Energy Agency, 2-4 Shirakata, Tokai-mura, Naka-gun, Ibaraki 319-1195, Japan

* Author to whom any correspondence should be addressed.

E-mail: takatori@okayama-u.ac.jp

Keywords: solid-state nuclear clock, thorium-229, XAFS

Abstract

Recent advancements in laser excitation of the low-energy thorium-229 (²²⁹Th) nuclear isomeric state in calcium fluoride (CaF₂) single crystals render this system a promising candidate for a solid-state nuclear clock. Nonetheless, the precise experimental determination of the microscopic ion configuration surrounding the doped ²²⁹Th and its electronic charge state remains a critical challenge. Such characterization is essential for precisely controlling the clock transition and evaluating the performance of this solid-state nuclear clock system. In this study, we use x-ray absorption fine structure spectroscopy of ²²⁹Th:CaF₂ to investigate the charge state and coordination environment of doped ²²⁹Th. The results indicate that ²²⁹Th displays a 4+ oxidation state at the substitutional site of a Ca²⁺ ion, with charge compensated provided by two F[−] ions positioned at interstitial sites adjacent to ²²⁹Th.

1. Introduction

Thorium-229 (²²⁹Th) possesses an isomeric nuclear state with an exceptionally low excitation energy of 8.4 eV, which can be accessed using laser light at a wavelength of 148 nm in the vacuum ultraviolet (VUV) range. The unique nuclear transition of the ²²⁹Th isomeric state (^{229m}Th) facilitates the development of a nuclear clock. Solid-state nuclear clocks using ²²⁹Th-doped crystals enable the simultaneous interrogation of numerous nuclei, offering significant advancements in fundamental physics and practical applications as stable clocks with reduced averaging times [1–3]. Recent studies have demonstrated the direct laser excitation of ²²⁹Th from its ground state [4–6], further advancing the realization of solid-state nuclear clocks. However, the mechanisms and properties governing the de-excitation of ^{229m}Th in the solid state remain inadequately understood. The de-excitation process can exhibit significant variation depending on the electronic state of ²²⁹Th within the crystal, potentially involving pathways such as radiative decay, internal conversion [7], and bound internal conversion [8]. A detailed understanding of the microscopic properties of crystals doped with ²²⁹Th, particularly the suppression of non-radiative decay channels, is critical for the practical realization of a solid-state nuclear clock. The nuclear clock transition frequency in ²²⁹Th-doped crystals incorporates an interaction between the nuclear quadrupole moment and the electric field gradient (EFG), causing hyperfine splitting [3]. The EFG at the ²²⁹Th nucleus is determined by the configuration of the surrounding ions and can be enhanced by deformation of the thorium atom's electron shell ('Sternheimer antishielding' [9]).

Experimental determination of the local atomic structure surrounding the ^{229}Th site and the charge state of the ^{229}Th is crucial for evaluating the performance potential of a solid-state nuclear clock.

Among potential nuclear clock materials, thorium-doped calcium fluoride crystals ($\text{Th}:\text{CaF}_2$) have been extensively studied [10–12] and are considered highly promising candidates. Isomer excitation experiments conducted with $^{229}\text{Th}:\text{CaF}_2$ have demonstrated narrow spectroscopic linewidths and reported long isomer half-lives (extrapolated to vacuum) as 1740(50) s [4], 1793(144) s [13], and 1770(12) s [6]⁷. These values are close to the measured half-life of 1400^{+600}_{-300} s using trapped $^{229}\text{Th}^{3+}$ ions [14] and fall within the theoretically estimated range of 10^3 – 10^4 s [15, 16]. This result suggests the absence, or significant suppression, of non-radiative decay channels in this material. However, ongoing discussions persist regarding isomer quenching during the pumping process [4, 13] and the competition between radiative and non-radiative decay channels [4, 17]. In ionic crystals such as CaF_2 , a Th dopant atom can substitute a Ca^{2+} cation with a charge state of $4+$ [10], similar to the stable electron configuration of the optically inert [Rn] noble gas. The lack of energetically accessible electronic states below 8.4 eV helps suppress non-radiative decay of the isomer, a critical requirement for the operation of the nuclear clock [18]. Several compensation mechanisms that consider the difference in the electrical charge between Ca^{2+} and Th^{4+} have been proposed. For example, the presence of two additional F^- ions at interstitial lattice sites (with two possible spatial arrangements possible), Ca^{2+} ion vacancies, or the incorporation of impurity O^{2-} ions. Structural characterization of high-concentration $^{232}\text{Th}:\text{CaF}_2$ using x-ray diffraction (XRD) has been reported in [12]. Although a direct signature of the Th dopant has yet to be observed, an overall increase in the CaF_2 lattice spacing on the 0.1 % level is attributed to the presence of the Th dopant. Comparison with theoretical simulations identifies a compensation model involving two interstitial F'_i ions arranged linearly as $\text{F}'_i\text{-Th-F}'_i$ as the most likely cause. However, the results from precision laser spectroscopy of the nuclear quadrupole splittings in $^{229}\text{Th}:\text{CaF}_2$ by [6] indicates a significant electric field anisotropy and hence a defect geometry that deviates considerably from the cubic lattice symmetry of CaF_2 . Furthermore, the ^{229}Th dopant isotope requires careful investigation, as its radioactivity may influence the formation of defect structures during and after crystal growth [19].

In this study, we employed x-ray absorption fine structure (XAFS) spectroscopy [20] to determine the valency and spatial arrangement of the dominant thorium charge compensation mechanism in CaF_2 crystals. XAFS, utilizing the fluorescence yield method, was particularly suited for this investigation, as it allows for sensitive measurements even in dilute samples, such as ^{229}Th -doped crystals.

2. $^{229}\text{Th}:\text{CaF}_2$ crystal

2.1. Crystal development

The TU Wien group established the growth of $^{229}\text{Th}:\text{CaF}_2$ single crystals with high doping concentrations (10^{17} – 10^{19} / cm^3) and high VUV transmission [19, 21]. The crystal fabrication process utilizes the vertical gradient freeze method, which can be summarized as follows: The doping material $^{229}\text{ThF}_4:\text{CaF}_2$ is placed into a pocket at the top of a CaF_2 single bulk seed crystal (a 3.2 mm diameter cylinder with a height of 11 mm), under vacuum conditions to prevent oxidation. A steep temperature gradient is applied to the dopant powder and the seed crystal to locally melt the material from the top when the temperature reaches 1691 K. The liquid–solid interface is controlled by adjusting the temperature gradient to melt the top 5 mm of the seed crystal, which contains the doping material. Subsequently, the overall temperature is gradually reduced over several days, allowing the single crystal to form atop of the seed. To enhance the VUV transmittance, the crystals are re-heated to 1423 K at ambient pressure under a CF_4 atmosphere to reverse the fluoride deficiency caused by ^{229}Th radioactivity induced radiolysis during crystal growth.

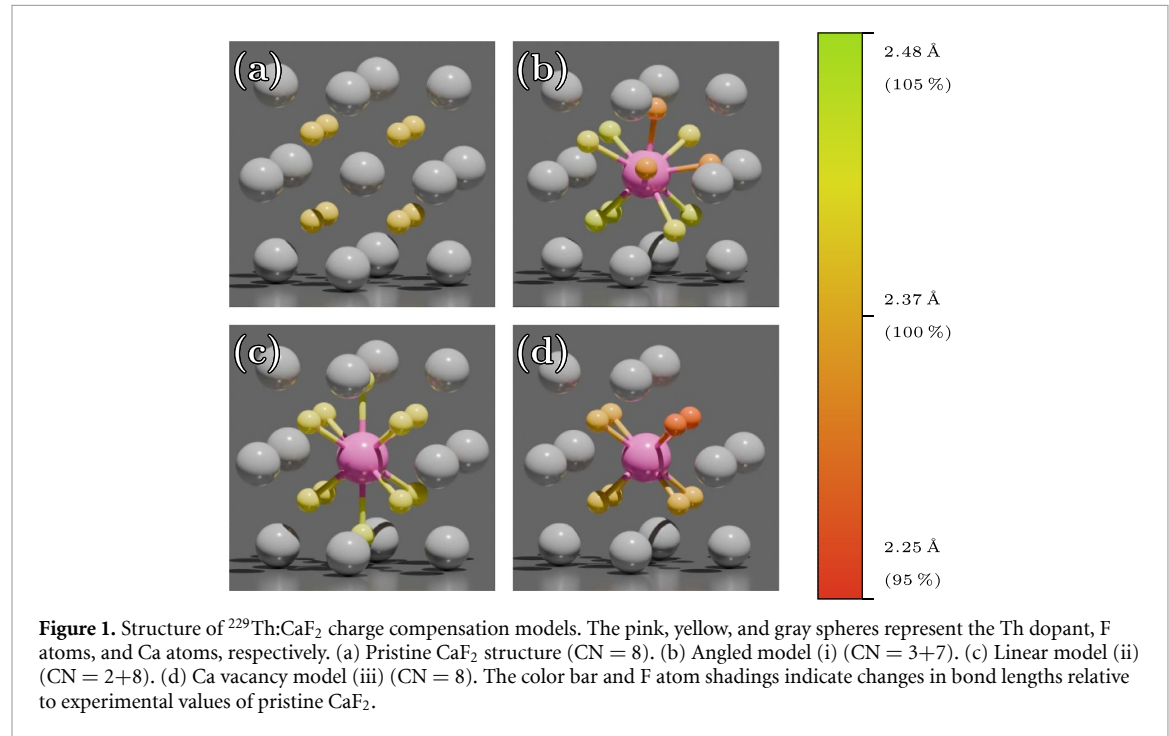
2.2. Structural models

To theoretically describe the $^{229}\text{Th}:\text{CaF}_2$ crystal structure, we conducted simulations using the Vienna ab-initio simulation package (VASP) [22–26], employing density functional theory (DFT), and using the generalized gradient approximation by Perdew *et al* [27] (PBE-GGA) for the exchange-correlation potential. Candidate defect geometries were selected based on their influence on the optical (VUV) transmission of the doped crystal. Experimentally, only a slight reduction in the band gap was observed for $^{229}\text{Th}:\text{CaF}_2$, even at high doping concentrations up to the percent level [12, 19]. Fully charge-compensating defects, such as two fluorine interstitials or a single calcium vacancy, were demonstrated to retain high VUV transmission in DFT simulations [10, 11]. Open-shell, only partially compensated configurations, were excluded from consideration due to their poor optical transmission in the VUV region [11]. Additionally, defect schemes

⁷ The reported lifetime of 641(4) s in the CaF_2 crystal [6] was converted to a half-life in vacuum using the refractive index $n = 1.586$ at 148.4 nm.

Table 1. Charge compensation models investigated in this study: Models (i) and (ii) including 2 F_i' and one model (iii) including a Ca vacancy. Fluoride coordination numbers (CN) differ for various compensation types.

Model	Charge compensation	CN
(i) F_i angled	2 F_i' (F_i' -Th- F_i' : 71.09°, non-symmetric)	3+7
(ii) F_i linear	2 F_i' (F_i' -Th- F_i' : 180°, symmetric)	2+8
(iii) Ca vac	1 V_{Ca}'' (nearest-neighbor)	8



involving oxygen [10] were also discarded from the further analysis, as they were predicted to result in significant band gap reduction. We selected the initial positions for interstitial F_i' ions based on the symmetry of the pure CaF_2 cubic cell (space group $\text{Fm}\bar{3}\text{m}$, lattice constant 5.46 Å [28]). Interstitial fluorines have a maximal distance to fluorines from the lattice at Wyckoff positions 4b (assuming Ca occupies 4a sites). This placement ensures reasonable initial interatomic forces. In a CaF_2 supercell, this limits the 2 F_i' arrangements (in Kröger-Vink notation [29]) to two configurations with angles of 90° and 180° between the F_i' . We considered the nearest-neighbor Ca vacancy V_{Ca}'' for this stoichiometry (C_{2v} point group symmetry), as previous calculations showed an unfavorable defect formation energy for the *next-nearest* neighbor vacancy [30].

Before relaxation, all atoms were displaced by a negligible, random amount to completely break the lattice symmetry. Subsequently, we relaxed $2 \times 2 \times 2$ doped supercells of the conventional CaF_2 unit cell (corresponding to a doping concentration of $\text{Th}/\text{Ca} = 1/31$) until all ionic forces were smaller than $10^{-3} \text{ eV Å}^{-1}$. The first Brillouin zone was sampled only at the Gamma point. To validate the results, we computed the phonon normal modes at $q = \Gamma$ using phonopy (version 2.24.2 [31, 32]) and considered the structure converged if, due to numerical instabilities, no more than three modes with an imaginary component to their frequency exist, with each such component being smaller than 0.1 THz. If this criterion was not satisfied, all atoms were shifted along the eigenvectors of the largest imaginary mode, and the relaxation procedure was repeated. Table 1 and figure 1 present the obtained structural models.

Within the 2 F_i compensation schemes, two stable geometries exist: an ‘angled’ configuration with three F ions forming a 71.09° trihedron near to the Th dopant (C_{3v} point group symmetry) (figure 1(b)), and a ‘linear’ configuration with two 2 F_i ousted outwards, aligned with the lattice symmetry (D_4) as F_i' -Th- F_i' at an angle of 180° (figure 1(c)). The angled configuration has a total energy 0.92 eV lower than the linear configuration, resulting in only a 0.18% formation probability for the linear configuration, based on the Boltzmann factor at the crystal’s melting/freezing temperature of 1691 K [21]. A previous study [10] reported that two fluorine interstitials form in a 90° configuration. However, subsequent research [11] revealed that breaking any symmetry restrictions on the defect allows the system to relax in an energetically favorable configuration where the two 2 F_i' interstitials align as the 71.09° trihedron.

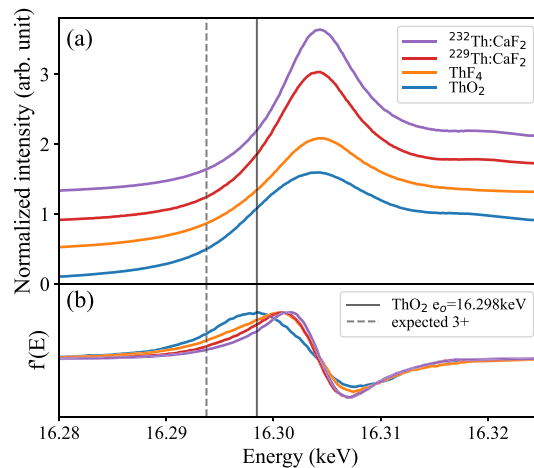


Figure 2. Thorium L_{III} edge XANES spectra of $^{232}\text{Th}:\text{CaF}_2$, $^{229}\text{Th}:\text{CaF}_2$, ThF_4 , and ThO_2 . (a) Normalized absorption edge spectrum. The background has been shifted along the vertical axis for clarity. (b) Derivatives of the absorption edge spectra. The solid vertical line depicts the absorption edge energy e_0 of ThO_2 . The dashed line depicts the absorption edge energy of Th^{3+} from [37].

3. XAFS measurements

XAFS measurements were conducted at the thorium L_{III} absorption edge (16.3 keV) at beamlines BL37XU and BL14B2 in SPring-8, Synchrotron Radiation Institute, Japan. We prepared two target samples: (A) $^{229}\text{Th}:\text{CaF}_2$ (^{229}Th is doped at a concentration of $4 \times 10^{17}/\text{cm}^3$) and (B) $^{232}\text{Th}:\text{CaF}_2$ (^{232}Th is doped at a concentration of $10^{19-20}/\text{cm}^3$), as well as two reference samples, $^{232}\text{ThO}_2$ and $^{232}\text{ThF}_4$. Details of the sample preparation and the experimental setup can be found in the appendix. The obtained XAFS data were analyzed in two energy regions: x-ray absorption near-edge structure (XANES) and extended x-ray absorption fine structure (EXAFS). Data analysis was conducted using the program Demeter [33] with background subtraction performed using typical Demeter procedures.

3.1. XANES measurements

The XANES spectra of the two target samples and the two reference samples were measured at beamline BL37XU, and are depicted in figure 2(a). The absorption edge position reflects the charge state of the Th atoms in each sample, generally shifting to higher energies with increasing ion valence [34, 35]. The absorption edge energies were determined based on the maximum of the first feature of the smoothed first derivatives of the XANES spectra (figure 2(b)), which is a standardized practice [36]. The Th dopant valence in ThO_2 and ThF_4 is 4+, and the ThO_2 edge position is indicated in figure 2. The absorption edge of Th^{3+} is also shown, citing [37] that reports that the charge state of Th in $\text{Th}_2@\text{C}_{80}$ is 3+ and its absorption edge is 4.7 eV lower than that of ThO_2 . Considering that the XANES peak shift of the target sample (A) is smaller than 3 eV, and does not shift below the energy of the ThO_2 peak, the valence of the ^{229}Th dopant is predominantly 4+. The absorption edge energy of target samples (A) and (B) did not differ considerably, suggesting that the radioactivity of ^{229}Th does not affect the ionic valence in the (re-fluorinated) crystal.

3.2. EXAFS measurement

In the EXAFS region, where the x-ray energy exceeds the absorption edge by more than 50 eV, inner shell electrons are emitted as photoelectrons. These photoelectrons scatter off neighboring atoms, generating an interference pattern on the top of the absorption edge that provides information about the atomic structure surrounding the Th atom. The interference pattern, denoted as $\chi(k)$ is regularly spaced in the wave number of the photoelectron k , which is defined as: $k \equiv \sqrt{2m(e - e_0)/\hbar}$, where m is the electron mass, e is the incident photon energy, and e_0 is the absorption threshold energy. Here, $\chi(k)$ is described using the EXAFS equation [38] as follows:

$$\chi(k) \propto \sum_j \frac{N_j e^{-2k^2 \sigma^2}}{k R_j^2} \sin(2k R_j + \delta_j(k)). \quad (1)$$

The index j represents the coordination shell of identical neighboring atoms positioned at approximately the same distance from the Th atom. Additionally, N_j denotes the number of neighboring atoms, and $\delta_j(k)$

Table 2. Best fit parameters and r -factors for models (i)–(iii). e_0 was fitted as a nonstructural parameter, and Δe_0 represents the energy shift from the theoretical e_0 value. $N_j^{\text{Th-F}}$ and $R_j^{\text{Th-F}}$ are values calculated from each structural model. $N_j^{\text{Th-F}}$ was fixed during fitting. R_j^{fit} represents the fitted Th–F bond distance.

Sample	Beam line	Model	Δe_0 (eV)	σ^2 (Å ²)	r -factor	$N_j^{\text{Th-F}}$ [$R_j^{\text{Th-F}}$ (Å)]	R_j^{fit} (Å)
(A). ²²⁹ Th:CaF ₂	BL37XU	(i) F _i angled	2.18 ± 1.23	0.004 ± 0.003	0.010	$N_1 = 3$ [$R_1 = 2.29$]	2.26 ± 0.04
						$N_2 = 7$ [$R_2 = 2.41$]	2.41 ± 0.01
		(ii) F _i linear	1.90 ± 1.75	0.007 ± 0.008	0.013	$N_1 = 2$ [$R_1 = 2.44$]	2.30 ± 0.24
						$N_2 = 8$ [$R_2 = 2.41$]	2.39 ± 0.02
		(iii) Ca vac	1.52 ± 2.61	0.002 ± 0.006	0.034	$N_1 = 2$ [$R_1 = 2.25$]	2.26 ± 0.11
						$N_2 = 6$ [$R_2 = 2.33$]	2.40 ± 0.02
(B). ²³² Th:CaF ₂	BL14B2	(i) F _i angled	2.43 ± 1.38	0.006 ± 0.004	0.007	$N_1 = 3$ [$R_1 = 2.29$]	2.28 ± 0.07
						$N_2 = 7$ [$R_2 = 2.41$]	2.40 ± 0.01
		(ii) F _i linear	1.23 ± 1.35	0.006 ± 0.003	0.006	$N_1 = 2$ [$R_1 = 2.44$]	2.25 ± 0.06
						$N_2 = 8$ [$R_2 = 2.41$]	2.39 ± 0.01
		(iii) Ca vac	1.46 ± 2.03	0.003 ± 0.004	0.013	$N_1 = 2$ [$R_1 = 2.25$]	2.26 ± 0.08
						$N_2 = 6$ [$R_2 = 2.33$]	2.40 ± 0.02

represents the phase shift. These parameters reflect the photoelectron scattering properties and represent the interference effects from the neighboring atoms. They can be calculated using the structural models described earlier. Here, R_j denotes the distance to the neighboring atom, and σ^2 is the variance in the distribution of neighbor-atom distances.

To investigate several structural models, we fit the observed fine-structure signal $\chi^{\text{data}}(k)$ using the EXAFS equation $\chi(k)$. The fitting focuses on the EXAFS signal from the F atoms surrounding the Th atom. In this process, we consider the signals from neighboring F atoms with similar Th–F bond lengths to be equivalent scatterers, using two different bond length scatterers: $j = 1$ and 2. The primary fitting parameters are R_1 , R_2 , and σ^2 . The EXAFS signal from the nearest-neighbor F atoms around Th appears as the main peak (two overlapping peaks for two bond distances) after Fourier transform (FT) from the $\chi^{\text{data}}(k)$ to the R -space. The workflow of the EXAFS data analysis is as follows: The EXAFS-related region is extracted from the entire background-subtracted and normalized observed signal using the FT window in k -space ($2.3\text{--}9.1 \text{ \AA}^{-1}$ was applied for sample (A)), and the extracted k -space data are Fourier transformed to obtain the R -space data. Subsequently, the fittings is performed on the main peak region of the EXAFS spectrum in the R -space ($0.9\text{--}3.0 \text{ \AA}$ applied before the phase $\delta_j(k)$ correction). The EXAFS spectrum for sample (A) measured at BL37XU in the R -space and the best fit for each model are depicted in figure 3(a). Figure 3(b) reveals the observed data obtained by inverse FT of the main peak to separate it from the second peak and the fitting results for each model in the k -space. Figure 3(c) compares of the residuals between the observed spectrum (main peak) and the models. Table 2 presents the parameters fitted by several models for both (A) and (B) samples.

3.3. Structure identification

All fitting results were evaluated using r -factor values [39], $\sum_{l=1}^n (\chi^{\text{data}}(r_l) - \chi^{\text{fit}}(r_l))^2 / \sum_{l=1}^n (\chi^{\text{data}}(r_l))^2$, where $\chi^{\text{data}}(r)$ is experimental data in R -space, $\chi^{\text{fit}}(r)$ is the result obtained by substituting the fitted parameters into the EXAFS equation, and n is the number of data points in the EXAFS fitting region. The smaller the r -factor is, the better is the goodness of fit. As depicted in table 2, structural models (i) and (ii) yield similar r -factors, whereas model (iii) exhibits poor fitting. Tendentially, sample (A) has a larger r -factors than sample (B) due to its lower doping concentration. Additionally, figure 3(c) demonstrates that the residuals between the observed data and the fitting in model (iii) are larger than those for the other models. This could be attributed to the model (iii)'s coordination number of eight, which does not accurately represent the experimental data. Therefore, we exclude the Ca vacancy model (iii) from further analysis. The primary feature that distinguishes the two F_i' interstitial models, (i) and (ii), is the Th–F bond distances, which strongly depends on the arrangement of the two additional F_i' and the relaxation of the atomic positions. Although stoichiometrically identical, these configurations differ qualitatively, as shown in figure 1: in the model as depicted in figure 1(b), three F atoms form a trihedron closer to the Th dopant (Th–F distance reduced compared to pristine CaF₂) while seven are slightly pushed out. In the model (ii), as depicted in figure 1(c), two F interstitials form a line along the crystal symmetry axis with an extended Th–F distance, whereas the usual eight nearest-neighbor F atoms remain essentially unaffected. Figure 4 presents the Th–F bond distances (R_1 and R_2) obtained from the best-fitting results in table 2. The Th–F bond distances derived from the fittings of model (i) align with the predicted bond distances (R_1 and R_2) for this

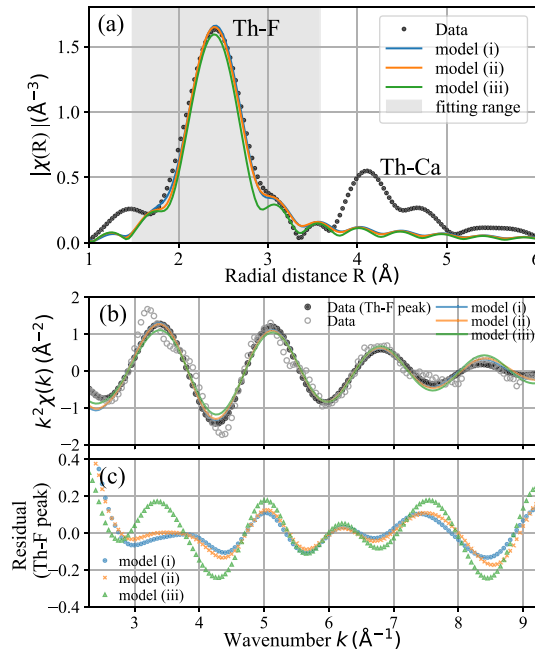


Figure 3. Thorium L_{III} edge EXAFS spectra of sample (A). (a) EXAFS spectra in the R -space. Phase $\delta_j(k)$ correction was applied based on the structural model. The main peak corresponds to the signal from the nearest neighbor F atoms. The second peak arises from the next-nearest neighbor Ca atoms. The model fitting of the EXAFS spectra was performed around the main peak (gray area). (b) EXAFS signal (Data), inverse Fourier transformed EXAFS signal (Data (Th-F peak)) for the main peak in R -space, and the model fitting results displayed in the k -space. (c) Residuals obtained by subtracting the fitting results from the observed EXAFS data (Th-F peak).

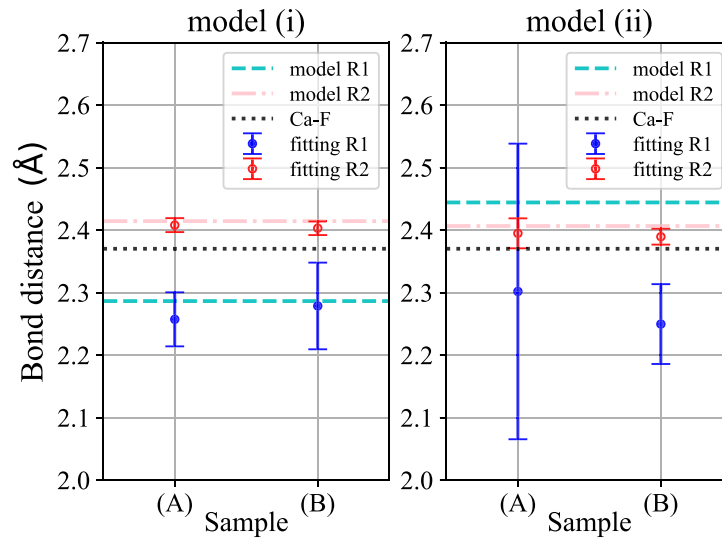


Figure 4. Fitting results of the Th-F bond distances (R_1 and R_2) summarized in table 2 are shown as points with error bars. The bond distances (R_1 and R_2) predicted by models (i) and (ii) are depicted as dashed lines. The Ca-F bond distance for undoped CaF_2 (2.37 Å [41]) is presented as a black dotted line.

model. By contrast, the fitting results of R_1 for model (ii), which describes the extended bond distance between Th and the two in-line F interstitial atoms, deviates considerably from the model prediction. We presume that model (i) more accurately describes the dominant Th defect structure in CaF_2 compared with model (ii). As for the valence state, considerable differences were not observed between samples (A) and (B). An obvious EXAFS signal was not observed at 3.595 Å [40], corresponding to the Th-Th distance in metallic thorium. Therefore, we exclude Th clustering or formation of Th nanoparticles in the CaF_2 crystals. Most of the discrepancies between the model fitting and the data shown in figure 3(c) are likely attributable to uncertainties in the estimation of the amplitude reduction factors (appendix C), the low concentration of sample (A) or noise. In this study, we identified a dominant defect type in the CaF_2 crystal. However, secondary or multiple secondary defect types are may also be present. Indeed, the recent laser spectroscopy

experiment [6] reported a weak splitting component that could not be attributed to any known defect. Since the EXAFS signal averages over all defect structures in the crystal, slight discrepancies may arise when fitting the data with a model that assumes only a single defect type.

4. Summary

Using the XAFS method, we confirmed that the ionic valence of ^{229}Th in the $^{229}\text{Th}:\text{CaF}_2$ crystal is $4+$ and that it is doped at the Ca^{2+} position. Additionally, we evaluated several theoretical models based on the EXAFS spectra. The experimental data suggest that ^{229}Th is charge-compensated by two F'_i , located at interstitial sites, with increased plausibility for a trihedral configuration of three F atoms compared to a linear alignment. This conjecture is further supported by the strong EFG asymmetry measured in spectroscopy of the nuclear quadrupole splittings in $^{229}\text{Th}:\text{CaF}_2$ [6]. The present study provides crucial insights into the practical applications of nuclear clocks by evaluating the characteristics of ^{229}Th in solid-state crystals. The evaluation method, which assesses both the ionic valence and local structure, is essential for determining the performance of solid-state nuclear clocks. This approach can be readily applied to various host materials, offering broad potential for future research.

Data availability statement

All data that support the findings of this study are included within the article (and any supplementary files).

Acknowledgments

The experiments were conducted at SPring-8 at the BL14B2 and BL37XU beamlines with the approval of the Japan Synchrotron Radiation Research Institute (JASRI) (proposals 2022B1936, 2023A1415, 2023B1447, and 2023B1890). We thank all the members of the SPring-8 operation and the supporting teams. This study was supported by JSPS KAKENHI Grant Nos. JP21H04473, JP22K20371, JP23K13125, JP24K00646, JP24KJ0168, and JP24H00228, and supported in part by ‘Initiative for Realizing Diversity in the Research Environment’ from MEXT. The results of this study were funded by the Okayama University Dispatch Project for the Female Faculty. This study work was funded by the European Research Council (ERC) under the European Union’s Horizon 2020 research and innovation programme (Grant Agreement Nos. 856415 and 101087184) and the Austrian Science Fund (FWF) [Grant DOI: <http://doi.org/10.55776/F1004>, <http://doi.org/10.55776/J4834>, <http://doi.org/10.55776/PIN9526523>]. This work was also supported by JSPS Bilateral Joint Research Projects No. 120222003. The author was able to write this paper thanks to the opportunity provided by TES–XAFS experiment. The author would like to thank Prof. S Yamada for his support. The author would like to thank Prof. H Abe for the helpful discussions. The computational results presented have been achieved in part using the Vienna Scientific Cluster (VSC).

Appendix A. Sample preparation

We prepared two types of thorium-doped target samples with thorium using the development method described in the section 2.1. Sample (A): $^{229}\text{Th}:\text{CaF}_2$ crystal. The crystal size is $2 \times 2 \times 1.2$ mm, and ^{229}Th is doped at a concentration of $4 \times 10^{17}/\text{cm}^3$ (an activity is 5 kBq). Sample (B): $^{232}\text{Th}:\text{CaF}_2$ crystal. Sample (B) was of two forms. The first was a single crystal with $1 \times 1 \times 1$ mm, dimensions, doped with ^{232}Th at a concentration of $2 \times 10^{19}/\text{cm}^3$. A pellet was also used to mitigate glitches caused by Bragg reflections when varying the incident x-ray energy on the single crystal. The pellet was made by grinding a $^{232}\text{Th}:\text{CaF}_2$ crystal doped with ^{232}Th at a concentration of $2 \times 10^{20}/\text{cm}^3$ into 150 mg of powder, mixing it with 150 mg of cellulose, and then pressing it into a shape with a diameter of ϕ 10 mm and a thickness of 1 mm. Additionally, the following two reference samples were used: Sample (C): $^{232}\text{ThO}_2$, with a pellet size of ϕ 13 mm \times 0.4 mm, containing 8.5 mg of $^{232}\text{ThO}_2$ diluted in 150 mg of cellulose. Sample (D): $^{232}\text{ThF}_4$, with a pellet size of ϕ 13 mm \times 0.5 mm containing 9.5 mg of $^{232}\text{ThF}_4$ diluted in 150 mg of cellulose.

Appendix B. Experimental setup

Sample (A) and sample (B) (single crystal) were measured at the BL37XU beamline at SPring-8. The BL37XU features an x-ray monochromator with a channel-cut Si(111) crystal and an undulator, providing a high beam intensity of 10^{12} photons/s. The measurements were conducted in the fluorescence mode at room temperature by using a nine-channel Ge detector. To mitigate glitches, a rotating stage was used (one rotation

per data point), with measurements conducted along the x-ray beam axis at angles ranging from 43 to 53°. The combination of a high-intensity beam and the rotating stage enabled the acquisition of XAFS data from a dilute $^{229}\text{Th}:\text{CaF}_2$ single-crystal sample. The energy was calibrated using the Sr *K*-edge, Y *K*-edge, and Zr *K*-edge. Sample (B) (high-concentration pellet) was measured at the BL14B2 beamline, primarily to validate the EXAFS spectrum. BL14B2 was equipped with an x-ray monochromator using a bending Si(311) crystal, with a beam intensity of 10^{10} photons/s. The sample was measured in the fluorescence mode using a 19-channel Ge detector. The energy was calibrated using the Sr *K*-edge. For both beamline measurements, reference samples (C) and (D) were used. These reference samples were measured in the transmission mode using two ion chambers.

Appendix C. EXAFS analysis

The fine-structure signal was modeled using the following EXAFS equation [38]:

$$\chi(k) = S_0^2 \sum_j \frac{N_j f_j(k) e^{-2k^2 \sigma_j^2}}{k R_j^2} \sin(2kR_j + \delta_j(k)).$$

Here, k is the wave number of the ejected photoelectron, and the index j refers to the shell number. The coordination number of the neighboring atoms, N_j , the back-scattering amplitude factor, $f_j(k)$, and the phase shift, $\delta_j(k)$, describe the photoelectron scattering properties of the neighboring atoms of the absorption atom. The N_j , $f_j(k)$ and $\delta_j(k)$ values were determined using the multiple-scattering calculation code FEFF [42–44]. The effect of the mean free path of the photoelectron is considered as part of the factors $f_j(k)$ and $\delta_j(k)$.

The amplitude reduction factors, S_0^2 , used in the model fitting were set to 0.93 at BL37XU and 1.16 at BL14B2, based on the EXAFS data fitting results from the ThO_2 reference sample ($S_0^2 = 0.93 \pm 0.22$ and $S_0^2 = 1.16 \pm 0.13$). The observed fine-structure signals were normalized after removing the atomic absorption background by using the AUTOBK algorithm [45]. When analyzing the observation data, the k -space FT window was adapted to the range of 2.3–9.1 \AA^{-1} for sample (A) and 2.3–10.2 \AA^{-1} in sample (B) to isolate the EXAFS signal from the observed data. Subsequently, the obtained R -space spectrum obtained by FT was fitted around the EXAFS signal corresponding to the main peak (Th–F), with a fitting range of 0.9–3.0 \AA for sample (A) and 1.1–2.4 \AA for sample (B). The fitting results around the main peak, as discussed in the section 3.2, are consistent with model (i), where two F'_i atoms are positioned at interstitial sites, forming a triangular arrangement with three F atoms. Additionally, we extended the fitting to include the range covering the second peak (Th–Ca), which was 0.9–3.9 \AA for sample (A) and 0.9–4.0 \AA for sample (B). The results, as shown in table C1, was also consistent with the bond lengths predicted by the model (i).

Table C1. Best fit parameters and r -factors for model (i). e_0 was fitted as a nonstructural parameter, and Δe_0 is the energy shift from the theoretical e_0 value. N_j and R_j^{model} are the coordination numbers and bond distances of the Th–F and Th–Ca bonds calculated from each structural model. N_j was fixed for fitting. R_j^{fit} is fitting results.

Sample	Beam line	Δe_0 (eV)	σ^2 (\AA^2)	r -factor	N_j [R_j^{model} (\AA)]	R_j^{fit} (\AA)
(A). $^{229}\text{Th}:\text{CaF}_2$	BL37XU	3.22 ± 1.66	0.005 ± 0.006	0.022	$N_1^{\text{Th-F}} = 3$ [$R_1^{\text{Th-F}} = 2.29$]	2.28 ± 0.09
					$N_2^{\text{Th-F}} = 7$ [$R_2^{\text{Th-F}} = 2.41$]	2.42 ± 0.01
					$N_3^{\text{Th-Ca}} = 3$ [$R_3^{\text{Th-Ca}} = 3.82$]	3.74 ± 0.08
					$N_4^{\text{Th-Ca}} = 9$ [$R_4^{\text{Th-Ca}} = 3.95$]	3.97 ± 0.04
(B). $^{232}\text{Th}:\text{CaF}_2$	BL14B2	2.57 ± 1.25	0.006 ± 0.004	0.023	$N_1^{\text{Th-F}} = 3$ [$R_1^{\text{Th-F}} = 2.29$]	2.28 ± 0.06
					$N_2^{\text{Th-F}} = 7$ [$R_2^{\text{Th-F}} = 2.41$]	2.40 ± 0.01
					$N_3^{\text{Th-Ca}} = 3$ [$R_3^{\text{Th-Ca}} = 3.82$]	3.75 ± 0.06
					$N_4^{\text{Th-Ca}} = 9$ [$R_4^{\text{Th-Ca}} = 3.95$]	3.97 ± 0.03

To assess the sensitivity of the EXAFS estimation to variations in the nearest neighbor distances, we scaled some distances in the structural model by factors ranging from 0.1 to 0.001 and fitted these adjustments to the EXAFS data. The results confirmed that the method is sensitive to distance deviations at the level of a few percent. After the structural optimizations in VASP, the cell volumes were slightly scaled (−1.98 %) to match the experimentally known lattice constant of CaF_2 (5.46 \AA), with no further relaxation of the lattice distance afterward. EXAFS fitting was also performed for model (i). The values $R_1 = 2.26 \pm 0.04$ \AA and $R_2 = 2.41 \pm 0.01$ \AA obtained from the fitting on sample (A) revealed high agreement with the model's values of $R_1 = 2.26$ \AA and $R_2 = 2.40$ \AA , as depicted in figure C1. This result further supports model (i), as it accounts for a known discrepancy in the lattice distances obtained from DFT compared to experimental values.

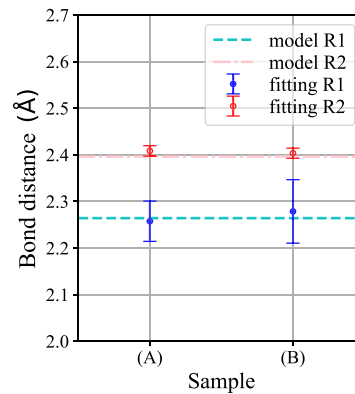


Figure C1. Fitting results of the Th–F bond distances of model (i) (R_1 and R_2) with lattice distances scaled in the structural model to match the experimentally determined values of CaF_2 are depicted as points with error bars. The coupling distances (R_1 and R_2) predicted by model are indicated as dotted lines.

Appendix D. Fluoride-deficient defects models

Based on the analysis of energy-stable states derived from first-principles calculations and the results of XANES measurements of Th dopant valence, the $2\text{F}_i'$ compensation model is strongly supported. However, assessing how effectively EXAFS data distinguishes (rejects) models without full F_i' compensation is also crucial. In addition to the $2\text{F}_i'$ model described in the section 2.2, we examined two fluoride-deficient models from fluorine loss (F_2) due to ^{229}Th radioactivity. The first model involves no F_i' compensation (model (iv)), whereas the second model includes only one F_i' compensation (model (v)). Model (iv) has a coordination number of eight (identical to pristine CaF_2), whereas model (v) has nine. Both models underwent structural relaxation as described in the section 2.2. Further details pertaining to these models are available in the literature [11, 30].

The EXAFS analysis results of the first peak (Th–F) indicate that model (iv), with no F_i' compensation, exhibits a high r -factor (0.055 for the sample (A) and 0.014 for the sample (B)), ruling out the absence of F_i' compensation. By contrast, model (v), with one F_i' compensation, presents relatively small r -factors of 0.021 for sample (A) and 0.008 for sample (B). However, the fitting results are $R_1 = 2.26 \pm 0.11 \text{ Å}$ ($N_1 = 2$), $R_2 = 2.40 \pm 0.02 \text{ Å}$ ($N_2 = 7$) for sample (A) and $R_1 = 2.25 \pm 0.06 \text{ Å}$ ($N_1 = 2$), $R_2 = 2.39 \pm 0.01 \text{ Å}$ ($N_2 = 7$) for sample (B). These results are inconsistent with the predicted neighboring atom distances ($R_1 = 2.30 \text{ Å}$, $R_2 = 2.45 \text{ Å}$). The fitting results suggest that the distances to all neighboring atoms are shorter, which can be attributed to the model's lower coordination number compared to the actual coordination number. Consequently, the EXAFS data analysis supports the $2\text{F}_i'$ compensation models over those with incomplete charge compensation. No significant differences were observed between $^{232}\text{Th}:\text{CaF}_2$ and the radioactive $^{229}\text{Th}:\text{CaF}_2$.

ORCID iDs

S Takatori <https://orcid.org/0000-0002-8705-9624>
M Pimon <https://orcid.org/0000-0001-7784-463X>
M Bartokos <https://orcid.org/0009-0004-7610-9122>
K Beeks <https://orcid.org/0000-0002-8707-6723>
T Hiraki <https://orcid.org/0000-0002-6235-5830>
A Leitner <https://orcid.org/0009-0007-1156-1881>
T Masuda <https://orcid.org/0000-0001-8122-5145>
F Schaden <https://orcid.org/0000-0001-7154-0440>
T Schumm <https://orcid.org/0000-0002-1066-202X>
T Sikorsky <https://orcid.org/0000-0003-0280-0928>
Y Takahashi <https://orcid.org/0000-0001-7860-2341>
T Yomogida <https://orcid.org/0000-0002-2005-0027>
A Yoshimi <https://orcid.org/0000-0002-2438-1384>
K Yoshimura <https://orcid.org/0000-0002-2415-718X>

References

- [1] Peik E and Tamm C 2003 *Europhys. Lett.* **61** 181
- [2] Rellergert W G, DeMille D, Greco R R, Hehlen M P, Torgerson J R and Hudson E R, 2010 *Phys. Rev. Lett.* **104** 200802
- [3] Kazakov G A et al 2012 *New J. Phys.* **14** 083019
- [4] Tiedau J et al 2024 *Phys. Rev. Lett.* **132** 182501
- [5] Elwell R et al 2024 *Phys. Rev. Lett.* **133** 013201
- [6] Zhang C et al 2024 *Nature* **633** 63–70
- [7] Seiferle B et al 2019 *Nature* **573** 243–46
- [8] Karpeshin F and Trzhaskovskaya M B 2017 *Phys. Rev. C* **95**
- [9] Feiock F D and Johnson W R 1969 *Phys. Rev.* **187** 39–50
- [10] Dessovic P et al 2014 *J. Phys.: Condens. Matter* **26** 105402
- [11] Pimon M, Grüneis A, Mohn P and Schumm T 2022 *Crystals* **12** 1128
- [12] Gong Q, Tao S, Zhao C, Hang Y, Zhu S and Ma L 2024 *Inorg. Chem.* **63** 3807–14
- [13] Hiraki T et al 2024 *Nat. Commun.* **15**
- [14] Yamaguchi A, Shigekawa Y, Haba H, Kikunaga H, Shirasaki K, Wada M and Katori H 2024 *Nature* **629** 62–66
- [15] Shigekawa Y et al 2021 *Phys. Rev. C* **104** 024306
- [16] Tkalya E V, Schneider C, Jeet J and Hudson E R 2015 *Phys. Rev. C* **92** 054324
- [17] Kraemer S et al 2023 *Nature* **617** 706–10
- [18] Peik E and Okhapkin M 2015 *C. R. Phys.* **16** 516–23
- [19] Beeks K et al 2024 *Phys. Rev. B* **109** 094111
- [20] Koningsberger D, Mojet B, van Dorssen G and Ramaker D 2000 *Top. Catal.* **10** 143–55
- [21] Beeks K et al 2023 *Sci. Rep.* **13**
- [22] Kresse G and Furthmüller J 1996 *Comput. Mater. Sci.* **6** 15–50
- [23] Kresse G and Furthmüller J 1996 *Phys. Rev. B* **54** 11169–11186
- [24] Kresse G and Hafner J 1993 *Phys. Rev. B* **47** 558–561
- [25] Kresse G and Hafner J 1994 *Phys. Rev. B* **49** 14251–14269
- [26] Kresse G and Joubert D 1999 *Phys. Rev. B* **59** 1758–1775
- [27] Perdew J P, Burke K and Ernzerhof M 1996 *Phys. Rev. Lett.* **77** 3865–3868
- [28] 2022 CaF₂ crystal structure: Datasheet from “pauling file multinaries edition – 2022” in springermaterials copyright 2023 Springer-Verlag Berlin Heidelberg & Material Phases Data System (MPDS), Switzerland & National Institute for Materials Science (NIMS), Japan
- [29] Kröger F and Vink H 1956 *Relations between the Concentrations of Imperfections in Crystalline Solids (Solid State Physics)* vol 3 (Academic Press)
- [30] Pimon M 2021 A density functional theory study of defects in large gap insulators *PhD Thesis* TU Wien
- [31] Togo A, Chaput L, Tadano T and Tanaka I 2023 *J. Phys.: Condens. Matter* **35** 353001
- [32] Togo A 2023 *J. Phys. Soc. Japan* **92** 012001
- [33] Ravel B and Newville M 2005 *J. Synchrotron Radiat.* **12** 537–41
- [34] Newville M 2004 Consortium for Advanced Radiation Sources, University of Chicago (USA)
- [35] Sanyal K, Khooha A, Das G, Tiwari M K and Misra N L 2017 *Anal. Chem.* **89** 871–6
- [36] Calvin S 2013 *XAFS for Everyone*
- [37] Zhuang J et al 2021 *Nat. Commun.* **12**
- [38] Lee P A and Pendry J B 1975 *Phys. Rev. B* **11** 2795–811
- [39] Hamilton W C 1965 *Acta Crystallogr.* **18** 502–510
- [40] James W J and Straumanis M E 1956 *Acta Crystallogr.* **9** 376–9
- [41] Saravanan R and Israel S 2004 *Physica B* **352** 220–6
- [42] Rehr J J, Mustre de Leon J, Zabinsky S I and Albers R C 1991 *J. Am. Chem. Soc.* **113** 5135–40
- [43] Zabinsky S I, Rehr J J, Ankudinov A, Albers R C and Eller M J 1995 *Phys. Rev. B* **52** 2995–3009
- [44] Rehr J J and Albers R C 2000 *Rev. Mod. Phys.* **72** 621–54
- [45] Newville M, Living P, Yacoby Y, Rehr J J and Stern E A 1993 *Phys. Rev. B* **47** 14126–31